

Vorticity Packing Effects on Turbulent Transport in Decaying 2D Incompressible Navier-Stokes Fluids.

Snehanshu Maiti,^{1, a)} Shishir Biswas,² and Rajaraman Ganesh^{1, 3}

¹⁾*Institute for Plasma Research, Bhat, Gandhinagar, Gujarat 382428, India*

²⁾*Department of Physics and Astronomy, University of Notre Dame, Notre Dame, IN, USA*

³⁾*Homi Bhabha National Institute, Training School Complex, Anushaktinagar, Mumbai 400094, India.*

(Dated: 12 September 2025)

This paper investigates the role of initial vorticity packing fractions on the transport properties of decaying incompressible two-dimensional Navier–Stokes turbulence at very high Reynolds numbers and spatial resolutions. Turbulence is initiated via the Kelvin–Helmholtz instability and evolves through nonlinear inverse energy cascades, forming large-scale coherent structures that dominate the flow over long eddy turnover times. The initial vorticity packing fraction and circulation direction lead to qualitatively distinct turbulence dynamics and transport behaviors. Tracer particle trajectories are computed in the fluid field obtained using the Eulerian framework, with transport and mixing quantified using statistical measures such as absolute dispersion, position probability distribution functions (PDFs), and velocity PDFs. In the early stages, the onset of turbulence is primarily governed by the instability growth rate, which increases with vorticity packing fraction. As the flow evolves, transport exhibits a range of behaviors—subdiffusive, diffusive, or superdiffusive—and transitions between anisotropic and isotropic regimes, depending on the initial vorticity packing, flow structure, and stage of evolution. At later times, transport is dominated by the motion of large-scale coherent vortices, whose dynamics are also influenced by the initial vorticity packing ranging from subdiffusive trapping rotational motion and random walks, and Lévy flight-like events. These findings offer insights into transport in quasi-2D systems—ranging from laboratory-scale flows to geophysical phenomena and astrophysical structures—through analogies with 2D Navier–Stokes turbulence.

I. INTRODUCTION

Two-dimensional (2D) turbulence exhibits rich and intriguing behavior, where nonlinear interactions drive both unique turbulent cascades and the formation of long-lived coherent structures^{1–3}, along with important scale-dependent transport properties⁴. Such dynamics plays a fundamental role across a wide range of physical systems—from laboratory to astrophysical scales—particularly in quasi-two-dimensional contexts where two spatial dimensions dominate over the third and the flow often exhibits a mixture of 2D and 3D characteristics.

In the laboratory, quasi-2D turbulent features arise in magnetically confined plasmas—such as those in Tokamaks^{5,6} and in non-neutral plasmas confined in Penning–Malmberg traps⁷—where strong magnetic fields suppress variations along field lines, giving rise to quasi-2D dynamics. In these systems, turbulent transport plays a crucial role in limiting confinement and overall device performance. On planetary scales, strong rotation gives rise to quasi-2D geostrophic flows that drive atmospheric⁸ and oceanic⁹ circulation and transport, with 2D turbulence features evident in Earth’s weather systems and even more prominently in the atmospheres of gas giants¹⁰. Understanding such flows is crucial for addressing environmental challenges, including pollutant transport and climate-related risks¹¹. At cosmic scales, signatures of 2D turbulence also appear in the formation of galaxies and galaxy

clusters¹². Across all these domains, understanding 2D turbulence offers fundamental insights into the emergence of large-scale flow structures and self-organization and their transport properties across a wide range of physical systems.

2D fluid turbulence refers to the chaotic, irregular motion of fluid in both spatio-temporal scales and constrained to a plane. Its dynamics, often driven by various instabilities, are marked by the formation, merging, and nonlinear interaction of circular and spiral-like vortices, leading to the development of large-scale flow structures and self-organization. A defining feature of 2D turbulence is the dual cascade phenomenon: an inverse energy cascade, which transfers energy from small to large scales, and a direct enstrophy cascade, which transfers mean-squared vorticity to smaller scales. This contrasts sharply with three-dimensional (3D) turbulence, where energy cascades predominantly from large to small scales. The distinct behavior in 2D flows stems from the simultaneous conservation of energy and enstrophy in the inviscid limit. As a result, large-scale coherent structures—such as long-lived vortices and jets—naturally emerge and tend to dominate the dynamics over time. These structures play a critical role in shaping the mixing and transport properties of 2D turbulent flows, with important real-world implications. The Antarctic circumpolar vortex is a key geophysical feature that shapes stratospheric ozone dynamics and drives the formation of the Antarctic ozone hole. Forming during winter, it effectively isolates polar air from mid-latitude air, and this isolation, combined with polar stratospheric clouds and the return of sunlight in spring, triggers rapid ozone depletion within the vortex¹³.

In fluid turbulence, the Eulerian framework focuses on the evolution of fluid quantities—such as velocity and vortic-

^{a)}Electronic mail: snehanshu.maiti@ipr.res.in

ity—at fixed spatial locations, whereas the Lagrangian framework tracks individual fluid parcels along their trajectories. The Lagrangian perspective offers direct insight into scale-dependent particle transport, dispersion, and mixing, and reveals the underlying structure of turbulence in the form of Lagrangian Coherent Structures (LCS)¹⁴. In 2D turbulence, long-lived rotating structures act as trapping regions that inhibit scalar advection across their boundaries, while saddle regions enhance dispersion by stretching fluid elements into thin filaments along unstable manifolds. This dynamic interplay leads to particle motion characterized by alternating trapping, random walks, and Lévy flight-like events. Foundational contributions include G.I. Taylor’s work on single-particle (absolute) dispersion¹⁵ and Richardson’s theory of two-particle (relative) dispersion¹⁶, both of which have been extended to multi-particle statistics^{17,18}. These approaches provide deeper insight into the geometry, transport, mixing, and intermittency of turbulent flows. In recent years, substantial progress has been made in characterizing Lagrangian chaos and the organizing structures within turbulence using tools such as finite-scale Lyapunov exponent (FSLE) analysis¹⁹ and finite-time Lyapunov exponent (FTLE) analysis^{14,20} and LCS identification¹⁴. Experimental, theoretical, and numerical studies have extensively investigated both Eulerian and Lagrangian approaches to 2D turbulence^{21–24}, and several comprehensive reviews are available²⁵.

A recent study investigated the influence of the initial vorticity packing fraction on the long-term behavior of two-dimensional incompressible decaying Navier–Stokes turbulence using high-resolution numerical simulations²⁶. This work emphasized the importance of understanding how the initial vorticity distribution impacts the late-time dynamics of 2D turbulence and its agreement with statistical mechanics predictions. In point vortex theory, statistical mechanical models treat vortices as discrete points, disregard incompressibility, and conserve only the total energy and zero total circulation, leading to the classical sinh–Poisson relationship²⁷ between vorticity and stream function. In contrast, the patch vortex theory treats vortices as finite-sized patches and by enforcing incompressibility through the conservation of regions with zero and nonzero vorticity, it predicts a generalized relaxed state described by the KMRS theory^{28–30}. This study reveals that, for systems with highly packed vortices, the late-time states are consistent with patch vortex theory, whereas a reduced packing fraction leads to late-time states that align with point vortex theory. This clearly demonstrates the crucial role of the initial vorticity packing fraction in determining the long-term behavior of 2D turbulent flows.

Building on earlier work that explored the role of initial vorticity packing on the long-term fluid dynamics, we extend the analysis by additionally examining the transport properties of the flow and identifying correlations between these two perspectives. In this study, we aim to investigate how varying initial vorticity configurations—specifically the vorticity packing fraction—affect transport dynamics in two-dimensional (2D) incompressible Navier–Stokes fluids. This parameter, despite its potential importance, has not been systematically explored to understand fluid transport properties. Our inves-

tigation is relevant for understanding a variety of quasi-2D systems, including geostrophic flows and plasma turbulence. We focus on freely decaying 2D turbulence, which—despite its spatiotemporal complexity—exhibits a remarkable degree of coherence²⁶. Emphasizing single-particle statistics, we analyze passive particle trajectories in an evolving turbulent velocity field, where the motion of tracer particles is strongly influenced by the inverse energy cascade and the emergence and evolution of coherent structures.

To this end, a dedicated tracer-particle solver has been developed, tested, and integrated with an existing in-house GPU-based 2D fluid code, GHD2D²⁶, designed for neutral fluids. The particle solver has been benchmarked against standard results from a 2D kinematic chaotic system³¹, ensuring its reliability. Using this combined tool, we investigate the transport properties of two-dimensional Navier–Stokes turbulent flows initiated by Kelvin–Helmholtz instabilities and allowed to decay freely. Particle transport is examined across short, intermediate, and long timescales. The nature of the resulting turbulence is modulated by varying the initial conditions, particularly the vorticity packing fraction at the initial time. To characterize the resulting transport, we compute the mean square displacement (MSD) of tracer particles over time, as well as the probability distribution functions (PDFs) of their positions and velocities. These diagnostics are used to correlate turbulent transport features with the initial vorticity distribution.

In Section II, we describe the numerical simulations and the governing equations employed in this study. Section III presents our results, highlighting several distinct regimes of fluid and particle motion that emerge during the evolution of turbulence, and how these regimes are influenced by the initial vorticity packing fraction. In particular, we report the mean square displacement of particles over time, as well as the probability distribution functions (PDFs) of particle positions and velocities along both spatial directions. These statistical measures offer valuable insights into the nature of the underlying turbulent structures and transport dynamics. Finally, in Section IV, we summarize our findings and present the main conclusions of the study.

II. EQUATIONS AND NUMERICAL SOLVERS

In this section, we present the governing equations, describe the numerical solvers we have used and their benchmarking, and detail the simulation setup and chosen parameters used to study two-dimensional (2D) fluid turbulence and its associated tracer particles transport.

Eulerian framework: Governing equations

The dynamics of incompressible 2D hydrodynamic turbulence in the absence of external forcing is governed by the dimensionless Navier–Stokes equation and the solenoidal condition:

$$\frac{\partial \vec{u}}{\partial t} + (\vec{u} \cdot \vec{\nabla}) \vec{u} = -\frac{\vec{\nabla} p}{\rho} + \frac{1}{R_E} \nabla^2 \vec{u}; \quad \nabla \cdot \vec{u} = 0 \quad (1)$$

where \vec{u} is the fluid velocity field, p is the fluid pressure, and ρ is the fluid density. All quantities in Eq. (1) are non dimensional. The Reynolds number, R_E , is a dimensionless parameter that quantifies the ratio of inertial to viscous forces, and is defined as $R_E = \frac{u_0 L_0}{\nu}$ where u_0 and L_0 are characteristic velocity and length scales, respectively, and ν is the kinematic viscosity. Larger values of R_E indicate a greater dominance of inertial effects over viscous effects, corresponding to more turbulent flow conditions.

To simplify analysis, the velocity field can be reformulated in terms of scalar quantities: the vorticity $\omega(x, y, t)$, representing local fluid rotation, and the stream function $\psi(x, y, t)$, which remains constant along the streamlines. This formulation yields the scalar vorticity equation:

$$\frac{\partial \omega}{\partial t} = [\psi, \omega] + \frac{1}{R_E} \nabla^2 \omega \quad (2)$$

The relationships among velocity, vorticity, and stream function are:

$$\omega = \hat{z} \cdot (\nabla \times \vec{u}); \quad \omega = -\nabla^2 \psi; \quad \vec{u} = \nabla \times \psi \quad (3)$$

where \vec{u} is the in-plane 2D velocity vector and \hat{z} is the out-of-the-board unit vector. Here, $[\psi, \omega]$ in Eq. (2) denotes the Poisson bracket, defined as:

$$[\psi, \omega] = \partial_x \psi \partial_y \omega - \partial_y \psi \partial_x \omega \quad (4)$$

The dynamics of incompressible two-dimensional (2D) Navier–Stokes fluids are typically initiated by an instability, leading to the evolution of the vorticity and stream function fields into a turbulent state through nonlinear interactions. This turbulence undergoes an inverse energy cascade, ultimately forming large-scale coherent structures. To reproduce this behavior, we solve the Naviers-Stokes equations and describe the corresponding numerical methods and setup in the following section.

Numerical setup

We have used an existing GPU-based incompressible two-dimensional hydrodynamic solver, GHD2D^{26,32}, developed in-house at the Institute for Plasma Research, to solve Eqs. (1)–(4) and study two-dimensional decaying fluid turbulence in a doubly periodic square domain with Cartesian coordinates. This solver is capable of performing state-of-the-art simulations at high grid resolutions (up to 2048^2)²⁶ and at very high Reynolds numbers (up to $228,576$)²⁶, both of which have been employed in our study. The solver employs the pseudospectral method, which represents the solution using global basis functions, such as Fourier modes in the case of periodic

domains. This approach leverages the high accuracy of spectral techniques for computing spatial derivatives, making it particularly well-suited for problems with periodic boundary conditions and smooth solution fields. While linear terms and derivatives are efficiently handled in spectral space, nonlinear terms are computed in physical space after performing an inverse Fast Fourier Transform (FFT). This hybrid treatment allows for computational efficiency while retaining spectral accuracy. To suppress aliasing errors that arise during nonlinear product evaluation, the standard 2/3 dealiasing rule³³ is applied, whereby the highest one-third of the spectral modes are set to zero. The time integration is carried out in spectral space using a second-order Adams–Bashforth method^{34,35}, ensuring stable and accurate evolution of the solution in time. The solver uses CUDA based FFT library [cuFFT library]³⁶ to perform Fourier transforms.

We generate various turbulent flow regimes using GHD2D at a high grid resolution of 2048×2048 by systematically varying the initial vorticity packing fraction, achieved through altering the number of initial vorticity strips in the simulation domain. The vorticity distribution is initialized using parallel, alternating strips of positive and negative vorticity, simulating oppositely directed jets. The number of strips is varied from 2 to 20. The computational domain is a square of size $L = 2\pi$, and each strip has a width $d = \pi/16$. The region between the strips is non-circulating (zero vorticity). The vorticity packing fraction (PF), defined as the ratio of the area occupied by circulating regions to the total domain area, is given by:

$$PF = \frac{n \cdot d \cdot L}{L^2} \quad (5)$$

where n is the number of strips. The packing fractions corresponding to 2, 4, 8, 16, and 20 strips are 6.25%, 12.5%, 25%, 50%, and 62.5%, respectively.

The circulation is defined as $C = \int \omega dx dy$. For the positive vorticity regions, the total circulation is:

$$C_+ = n_+ \cdot d \cdot L \cdot \omega_+ \quad (6)$$

Since the number of positive and negative strips is equal, we have $C_+ = C_-$, and thus the net circulation is $C = C_+ + C_- = 0$.

The system is perturbed by adding a small-amplitude perturbation to the vorticity field:

$$\delta \omega = \sum_{m=1}^{64} \alpha \cos(mx + \phi_m) \quad (7)$$

where α denotes the perturbation amplitude (assumed to be small), m is the mode number, and ϕ_m represents the phase associated with each mode. In our simulations, the perturbation amplitude α is set to 0.01. The phase ϕ_m is randomly drawn from a uniform distribution between $-\pi$ and π . The system is integrated with a time step of $\Delta t = 10^{-3}$, sufficient to resolve the dynamics at a resolution of 2048^2 , and evolved until $T = 3000$, at which point a

steady state is attained and examined over an extended period.

Benchmarking numerical simulations and study of Kelvin-Helmholtz instability

To validate the accuracy of our numerical simulations, we calculate the Kelvin-Helmholtz instability growth rates for a oppositely directed broken jet type initial configuration from our fluid simulations and compare them with well-established analytical results³⁷. The Kelvin-Helmholtz instability (KHI) is a hydrodynamic instability that occurs when there is a velocity difference across the interface between two fluids, or a velocity shear within a single fluid, leading to the formation of roll-up patterns and turbulence. The viscous growth rate of the Kelvin-Helmholtz instability for a step shear or broken jet profile in hydrodynamics, in the incompressible limit, was analytically derived by Drazin³⁷. The formula for the growth rate, as obtained by Drazin³⁷, is given as follows:

$$\gamma = \frac{k_x U_0}{3} \left[\sqrt{3} - 2 \frac{k_x}{R_E} - 2 \sqrt{\left(\frac{k_x}{R_E} \right)^2 + 2 \sqrt{3} \frac{k_x}{R_E}} \right] \quad (8)$$

where k_x is the dimensionless wave-number, U_0 is the dimensionless shear velocity and R_E denotes the Reynolds number. We compute the KHI growth rates for various mode numbers using our numerical simulations with the GHD2D code. In this setup, the initial condition consists of two oppositely directed jets (broken jets) with peak initial vorticities $\omega_0 = \pm 25$ and a tapered distribution profile to trigger the instability. In the tapered profile, the vorticity reaches its maximum at the center of the strips and decreases smoothly and symmetrically outward, resulting in a bell-shaped distribution instead of abrupt variations (see Fig. 1b). For a $R_E = 122$, the growth rate as a function of mode number from our simulations shows good agreement with the analytical predictions given by Eq. (8). This comparison is illustrated in Fig. 1a, where results from both low (grid size 256) and high (grid size 2048) resolution simulations are presented.

To bring out the insensitivity of our findings on the details of the initial vorticity profile, we explore the impact of the strip shape by comparing the tapered profile with a sharp-edged profile. In the sharp profile, the vorticity exhibits abrupt transitions between regions of high and low values, leading to steep gradients and a discontinuous-like structure. Figure 1b shows the vorticity distributions for both cases, configured with identical positions, widths, and circulations, and normalized to a lower peak value $\omega_0 = 1$ to facilitate the study of slower turbulence evolution. The resulting growth rates for both profiles at high R_E 228576 are compared in Fig. 1c, showing similar behavior. As expected, the KH (Kelvin-Helmholtz) growth rate for sharp-edged broken jet initial conditions is a bit higher than that for tapered-edge jets. The sharp-edge case is characterized by the introduction of strong shear layers at the jet boundaries, which generate a broader spectrum of unstable modes, particularly at smaller spatial scales (higher wavenumbers), due to the presence of discontinuous vorticity jumps. The high-wavenumber modes typ-

ically exhibit rapid growth, leading to a faster onset of the KH instability as compared to the other configuration. Consequently, the transition to turbulence is more rapid and efficient in the sharp-edge case. Based on this outcome, we choose to proceed with the sharp profile in subsequent studies.

We carry out additional investigations on the growth rate KH instability when we vary the R_E of the fluid and the number of strips in the initial condition and also the shape of initial profile and present in Fig 2. Fig 2a represents results from a tapered profile where we see that the growth rates increases with R_E . For a particular R_E while the growth rates are similar for instability generated by less number of strips 2, 4 and 8, they significantly increase for higher strip numbers 16 and 20. For the sharp profile case, with a $R_E = 228576$, we see that the growth rate increases with the number of strips (see Fig. 2b).

Tracer particle dynamics: Governing equations

The Lagrangian description involves tracking passive tracer particles that move with the flow but do not influence the fluid dynamics. The motion of such particles is governed by the following equations:

$$\frac{dx}{dt} = u(x, y, t) = \frac{\partial \psi}{\partial y}; \quad \frac{dy}{dt} = v(x, y, t) = -\frac{\partial \psi}{\partial x} \quad (9)$$

Here, $x(t)$ and $y(t)$ represent the instantaneous positions of the tracer particle as functions of time, $u(x, y, t)$ and $v(x, y, t)$ are the scalar fluid velocity field components in the x - and y -directions, respectively, and $\psi(x, y, t)$ is the stream-function field of the fluid, from which the incompressible velocity field is derived.

Numerical solver

To solve the above equations, Eq. (9), and to address the objectives of the present study, we have developed a custom particle-tracking solver to compute tracer particle trajectories from a given velocity or stream-function field. The advection equations are integrated using the fourth-order Runge-Kutta (RK4) algorithm, which has a local truncation error of $\mathcal{O}(h^5)$ and a global accuracy of $\mathcal{O}(h^4)$ ³⁸, and is chosen for its high accuracy and numerical stability. Particle trajectories are obtained using both velocity field and stream function interpolations, implemented via a linear interpolation scheme³⁸, with both methods yielding similar results for particle trajectories.

This particle solver has been integrated with the two-dimensional generalized hydrodynamics fluid code, GHD2D, allowing for simultaneous evolution of tracer particles and the underlying fluid flow. Simulations are performed over long durations (up to $T = 3000$ in simulation units) to ensure the system reaches a statistically steady state. The time step for both fluid and particle solvers is fixed at $\Delta t = 10^{-3}$. A total of 1000 tracer particles are employed to analyze dispersion characteristics.

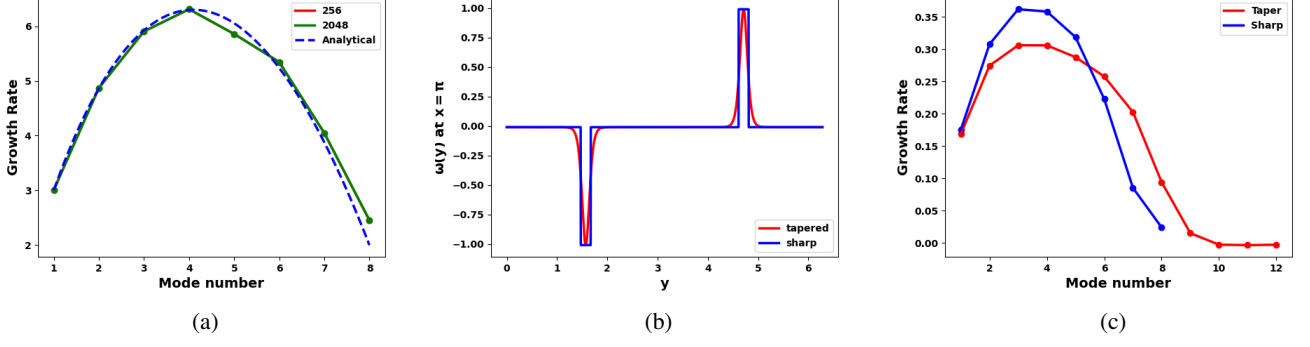


FIG. 1: Figure (a) shows the benchmarking of our GHD2D solver against the analytical results of Drazin et al., demonstrating close agreement in the growth rates of the Kelvin–Helmholtz instability across varying mode numbers for a 2 strip oppositely directed broken jet problem having a tapered vorticity distribution profile. The R_E of the fluid is 122, $\omega_0 = \pm 25$ and simulations has been performed at resolutions 256 and 2048. Figure (b) compares the vorticity profiles of the 2 strip oppositely directed broken jet problem implemented using sharp and tapered initial conditions. Figure (c) compares the growth rates of KH instability implemented using sharp and tapered initial conditions for a fluid with $R_E = 228576$ and $\omega_0 = \pm 1$ which shows comparatively similar behavior.

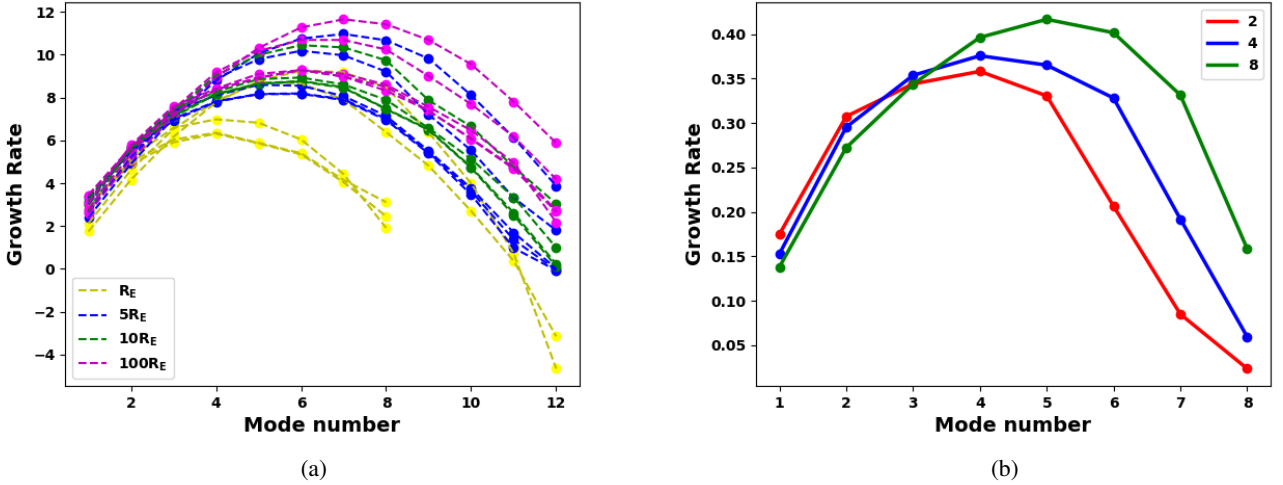


FIG. 2: Figure (a) shows the variation of Kelvin–Helmholtz instability growth rate with mode number for different combinations of Reynolds number ($R_E = 122$ and rest of them are multiples of this) and strip numbers (2, 4, 8, 16, 20) for a tapered profile of the initial vortex strips and vorticity $\omega_0 = \pm 25$. Each color in the plot denotes a distinct Reynolds number, and within each color group, different lines represent increasing vorticity strip counts (2 to 20); for a given R_E , the curves show an increasing trend with strip number. Each bell-shaped curve corresponds to a specific R_E –strip configuration, highlighting how both parameters influence the peak growth rate and the dominant mode. Figure (b) shows the same plots for a sharp profile of the initial vortex strips at a $R_E = 228576$ and $\omega_0 = \pm 1$.

Once particle trajectories are obtained, turbulent transport is quantified via ensemble-averaged tracer dispersion. The diffusion coefficients D_x and D_y in the x and y directions, along with the total diffusion D , are defined as:

$$D_x = \left\langle \frac{(x - x_0)^2}{2t} \right\rangle; D_y = \left\langle \frac{(y - y_0)^2}{2t} \right\rangle; D = D_x + D_y \quad (10)$$

where x_0 and y_0 denote the initial positions of the particles,

and $\langle \cdot \rangle$ indicates an ensemble average taken over all tracer particles. In addition to the diffusion characteristics given by Eq. (10), we also analyze the probability distribution functions of tracer positions, $n(x)$ and $n(y)$, and tracer velocities, $n(v_x)$ and $n(v_y)$, in each direction to gain further insight into transport and mixing in turbulent flows.

Numerical benchmarking

We benchmark our tracer particle code by simulating tracer particle transport in a kinematic two-dimensional chaotic flow, consisting of a regular lattice of non-stationary kinematic eddies, as studied by Forgia et al.³¹. The stream-function $\psi(x, y, t)$ and velocity $u(x, y, t)$, $v(x, y, t)$ representation of the flow is given as³¹:

$$\psi = \frac{\alpha}{k} \sin(k[x - \varepsilon \sin(\omega t)]) \sin(k[y - \varepsilon \sin(\omega t + \phi)]) \quad (11)$$

$$u = \alpha \sin(k[x - \varepsilon \sin(\omega t)]) \cos(k[y - \varepsilon \sin(\omega t + \phi)]) \quad (12)$$

$$v = -\alpha \cos(k[x - \varepsilon \sin(\omega t)]) \sin(k[y - \varepsilon \sin(\omega t + \phi)]) \quad (13)$$

The model setup in the reference problem consists of a square simulation box of length 2 km. The wavenumber is defined as $k = 2\pi/L = \pi \text{ km}^{-1}$, corresponding to an eddy size of $L/2 = 1 \text{ km}$. The maximum flow speed is set to $\alpha = 3.6 \text{ km/hr}$. The oscillation parameters of the stream function— ε , ω , and ϕ —are chosen to ensure a fully chaotic Lagrangian flow regime, with $\omega \approx \alpha/(2\pi k^{-1}) = 1.8 \text{ hr}^{-1}$, $\varepsilon = 0.2 \text{ km}$, and $\phi = 0$ for the simplest case. The spatial resolution is $\Delta x = 0.02 \text{ km}$, and the time step is $\Delta t = 10^{-3} \text{ hr}$ (i.e., 3.6 seconds). The simulation runs for a total of 100 hrs. Particle trajectories are computed using multiple methods: directly from the analytical velocity and stream-function fields, and via interpolation from both the velocity and stream-function fields, and the results are compared. We find that the transport obtained from all these methods is in close agreement. A total of 100 passive tracer particles are used in our simulation compared to 10000 particles used in the reference problem. In all cases, the dynamics exhibit ballistic behavior at short times, transitioning to normal diffusion at later times, with an eddy turnover time of approximately 1 hour. The overall transport characteristics of our simulations are consistent with the findings of Forgia et al.³¹ (see Fig. 3).

III. TURBULENT TRANSPORT

In this section, we discuss results obtained from numerical experiments exploring turbulent transport by varying the initial vorticity packing fraction (using 2, 4, 8, 16, and 20 strips), focusing on three regimes: linear growth, developing turbulence, and the steady-state dipole-forming phase. To understand transport across these regimes, we analyze absolute particle diffusion to capture dispersion and mixing, along with evolution of particle position and velocity distribution functions to characterize some aspects of the underlying dynamics. We begin by outlining general features of turbulence evolution, transport behavior, and associated distribution functions common across all vorticity packing fractions, and subsequently highlight key observations specific to each case.

We begin by describing the initialization of the 2D fluid and tracer particle system. At time $T = 0$, the fluid vorticity is arranged in alternating clockwise and anticlockwise circulation strips aligned along the x -direction. The number of strips

determines the initial vorticity distribution and packing fraction and influences the development of turbulence and coherent structures. Simultaneously, tracer particles are uniformly and randomly distributed across the 2D domain (see Fig. 4), resulting in flat and uniform position distribution functions in both the x and y directions (see $T = 0$, Fig. 7 and Fig. 9). All tracer particles start with the initial velocity of the fluid.

As the system evolves from $T = 0$, shear-driven coherent flows in the x -direction induce a left–right drift of tracer particles. This initial stage is characterized by linear fluid motion and ballistic tracer transport, with both motions primarily governed by the imposed shear flow. This ballistic motion leads to the most rapid and significant growth in x -direction transport—and in overall tracer displacement—observed throughout the entire evolution of the flow (see Fig. 11, 12b)). During this phase, total transport grows quadratically with time, dominated by tracer motion in the x -direction (see Fig. 5b), reflecting the influence of shear flow before vortex interactions and turbulent mixing set in. Correspondingly, the particle position probability density function (PDF) in x begins to broaden rapidly and moves beyond the box length, while the y -distribution remains nearly flat and confined within the box length, reflecting the shear driven anisotropic nature of early-stage transport (see $T = 30$ Fig. 7, 9)). Simultaneously, the tracer velocity distribution begins to evolve. The x -velocity, v_x distribution develops a bimodal structure, with peaks near the mean shear velocities of the oppositely directed jets, and exhibits limited spread beyond these values. In contrast, the y -velocity v_y distribution remains sharply peaked around zero, reflecting the onset of small transverse fluctuations that are only beginning to emerge (see Fig. 8, 10)).

This ballistic regime persists until shear amplifies small perturbations at the vorticity strip interfaces via the Kelvin–Helmholtz (KH) instability. Driven by the growing transverse kinetic energy (see Fig. 5a), the strip boundaries deform and roll up into coherent vortices (see $T = 30$, Fig. 6b). As vortex rolls begin to emerge, they interact with their nearest neighbors, marking the transition to nonlinear turbulence (see $T = 50$, Fig. 6c). The onset and character of these interactions are strongly influenced by the initial vortex packing fraction. A higher packing fraction results in more frequent and earlier interactions among vortex rolls, leading to an earlier onset of turbulence. The timescale of this transition is governed by the growth rate of the Kelvin–Helmholtz (KH) instability in the y -direction, which increases with packing fraction (see Fig. 5). During this transition period, the shear-driven linear motion is progressively suppressed by the emergence of instability-driven nonlinear dynamics in the y -direction, leading to vortex roll formation and interactions. As a result, x -direction transport slows down and becomes subdiffusive, while y -direction transport—initially exhibiting exponential growth—shifts to a superdiffusive regime. The total transport is governed by the combined evolution of x and y displacements. The degree of suppression in x -transport and the corresponding enhancement in y -transport are both strongly influenced by the initial vorticity packing fraction (see Fig. 11). As the vortices evolve and interact, the flow becomes increasingly chaotic, eventually transitioning into a fully tur-

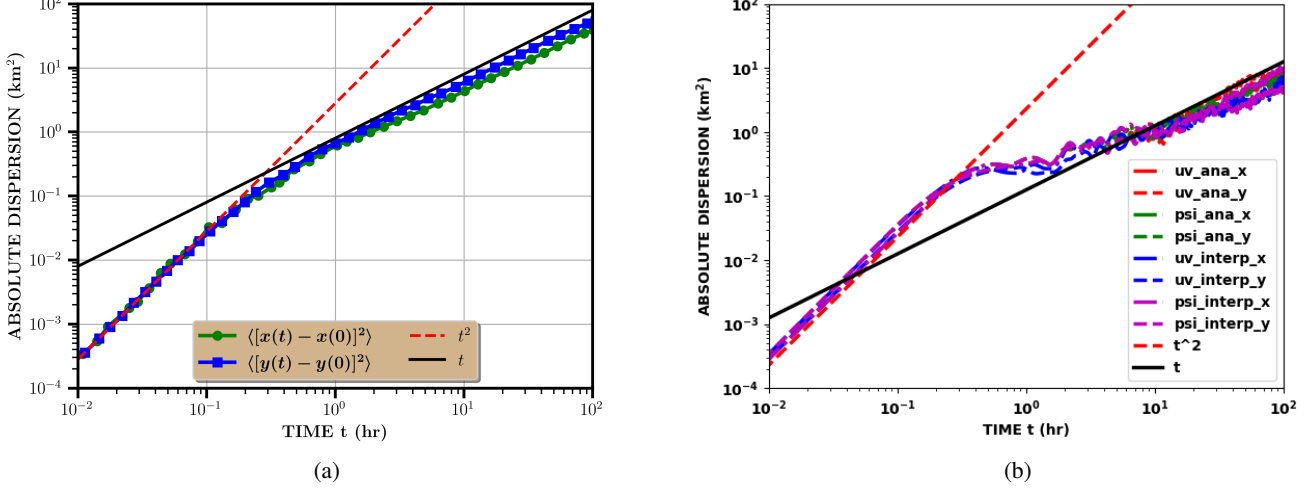


FIG. 3: Figure (a) shows the transport (absolute dispersion) of 10000 advected particles in a 2D kinematic chaotic flow composed of nonstationary regular lattices, as used by Folgia et al.³¹ (This figure has been reproduced from the results of Folgia et al., 2022³¹ with the corresponding author's permission). The transport initially follows a ballistic regime, transitioning into a normal diffusive regime. Figure (b) represents the transport results obtained from the particle solver used in the current study. 100 particles are used in the current benchmarking study and shows similar results like Figure (a) with initial ballistic regime transitioning into normal diffusive regime with a similar eddy turnover time of 1 hr.

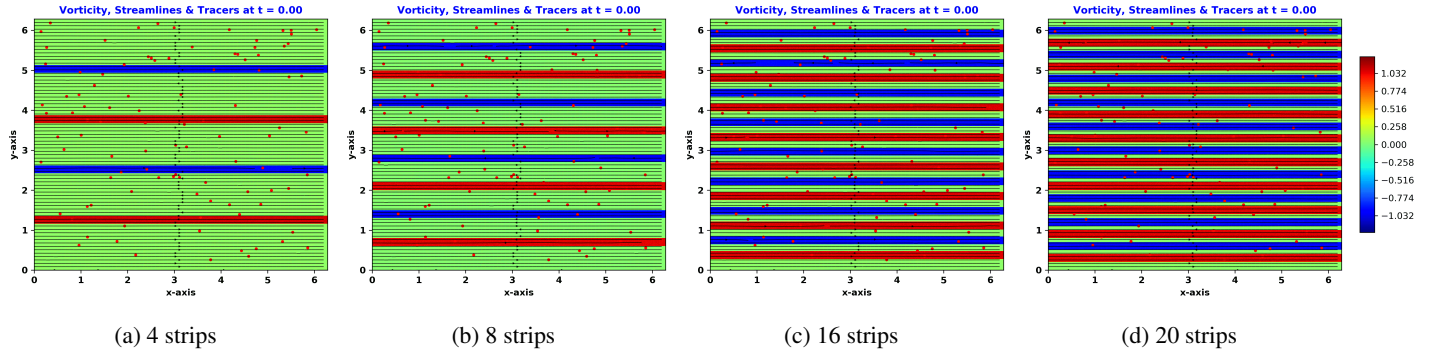


FIG. 4: This figure represents the initial vorticity and stream function distribution with associated tracers at $T = 0$ for various cases of turbulence to be generated. Figure (a) has low vortex packing fraction and has 4 strips whereas Figure (d) has highest vorticity packing fraction with 20 strips. The vorticity value for blue, red and green regions are -1, 1 and 0 respectively.

bulent regime. Tracer particles are advected in a seemingly stochastic manner, undergoing numerous small, random-like displacements driven by turbulent eddies. This motion resembles a random walk, causing the position probability distribution function (PDF)—particularly in the x -direction initially, followed by y —to approach a Gaussian shape (see $T = 50$, Fig. 7). The emergence of this normal distribution is explained by the central limit theorem, as the cumulative effect of many independent, small-scale fluctuations governs particle displacement. During this time, the y -velocity distribution broadens as small-scale, random perturbations emerge across multiple scales, gradually adopting a Gaussian shape. Meanwhile, the initially shear-dominated x -velocity distribution also begins to spread due to growing fluctuations, and progressively transi-

tions toward a normal distribution (see $T = 50$, Fig. 8).

Vortex rolls with the same sense of circulation tend to merge, deforming the surrounding fluid manifold in the process. This merging leads to the formation of progressively larger vortex structures, consistent with the inverse energy cascade characteristic of two-dimensional turbulence. As a result, the flow evolves into a complex state composed of a turbulent background interspersed with long-lived coherent structures, which together drive the dispersion and mixing of tracer particles (see $T = 100, 150, 200$, Fig. 6d, Fig. 6e, Fig. 6f). Notably, the cores of long-lived coherent structures often act as trapping regions, limiting scalar advection across their enclosing elliptic manifolds. In contrast, nearby hyperbolic saddle points enhance dispersion by stretching and deforming

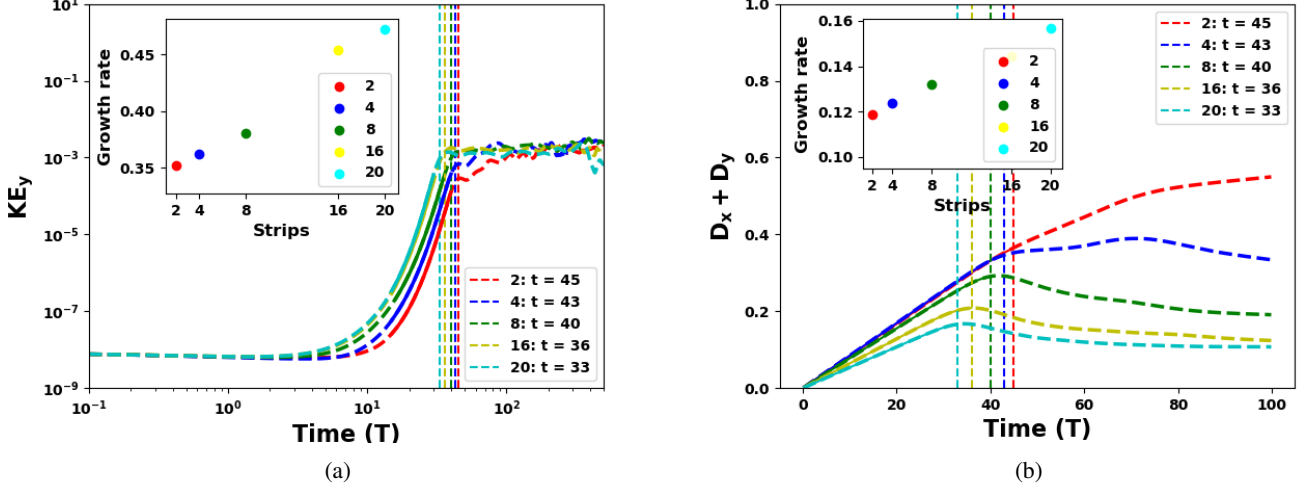


FIG. 5: (a) The y -direction kinetic energy (KE_y) evolution of the turbulent fluid initiated by varying initial circulation (strip numbers). The inset shows growth rates for different cases. (b) Transport evolution of passive tracers. Vertical lines in both indicate the transition from linear to nonlinear regimes.

fluid elements into elongated filaments along their unstable manifolds, thereby promoting mixing. The inverse cascade continues until the formation of large-scale dipolar vortices at late times ($T > T_D$), where the flow becomes increasingly dominated by these coherent dipoles (see $T = 1000, 2000$, Fig. 6h, Fig. 6i). After the onset of turbulence, the particle position distribution in the y -direction continues to broaden, transitioning into a super-diffusive regime and gradually approaching a Gaussian profile. This evolution eventually aligns the y -direction distribution with that of the x -direction in the high vortex packing case, marking the onset of isotropic turbulent mixing and transport (notably during $T = 50 - 500$), where $n(x) \approx n(y)$ (see $T = 500$, Fig. 9). In contrast, for lower vortex packing fractions, the system remains weakly anisotropic with $n(x) \geq n(y)$, indicating incomplete mixing and a directional bias in transport. During this phase, the broadening in the x -direction slows down as shear-driven motion is fully overtaken by turbulent dynamics. The velocity distributions in both x and y directions also evolve toward Gaussian forms, reflecting the influence of multiscale, random fluctuations characteristic of fully developed turbulence (see $T = 250$, Fig. 10).

These dipole structures primarily undergo circulatory motion, resulting in oscillatory trajectories in both the x and y directions, or in some cases, long-range flight events—reminiscent of Lévy flights—depending on the vorticity packing (see Fig. 11), which strongly influences the long-term dynamics of these dipoles. This interplay gives rise to a characteristic picture of two-dimensional turbulence, involving a combination of trapping, diffusion, and long-range flight events, where the presence and persistence of coherent structures play a significant role in the turbulent transport and mixing of passive scalars. Once the dipoles are formed, the particle position distributions in both the x and y directions become nearly Gaussian and remain symmetric, with close

overlap between the two directions over time (see $T = 2000, 3000$ Fig. 9). These dipoles are composed of two large, oppositely rotating vortices that remain spatially separated and coherent over long times. Their continued rotation causes tracer particles to circulate in opposite directions, maintaining two distinct populations of velocity states. As a result, the velocity distribution function tends to become bimodal again in this late-time regime. Each peak in the bimodal velocity PDF corresponds to one of the counter-rotating vortex populations, centered around $\pm v_{dp}$, where v_{dp} reflects the typical rotational velocity (see $T = 2000, 3000$ Fig. 10).

In the following sections, we discuss these dynamics in detail for varying vorticity packing fractions.

The **two-strip case** corresponds to the lowest vortex packing fraction, with only a few vortex rolls setting in due to the limited number of strips and their wide separation, resulting in a sparse and anisotropic configuration. Due to their wide spacing in the y -direction, these rolls evolve fully in an isolated manner and take comparatively longer to interact with neighbors, initially establishing unidirectional merging and fluid deformation primarily in the x -direction, driven by shear. As a result, turbulence sets in at a relatively late time ($T = 45$), leading to a relatively short-lived, weaker, and anisotropic turbulent background, along with the rapid formation of a few larger-scale coherent vortices. The inverse cascade proceeds until the formation of the largest-scale dipoles, occurring at $T = 400$. After the dipole formation, the dynamics is dominated by slowly drifting dipoles executing large-radius circular motions.

We discuss the transport of advected particles for this two strip case now. As the flow starts, the particle motion follows the initial shearing motion along x direction and is ballistic in nature. The shear-driven linear motion in the x -direction persists the longest, while instability-driven non-

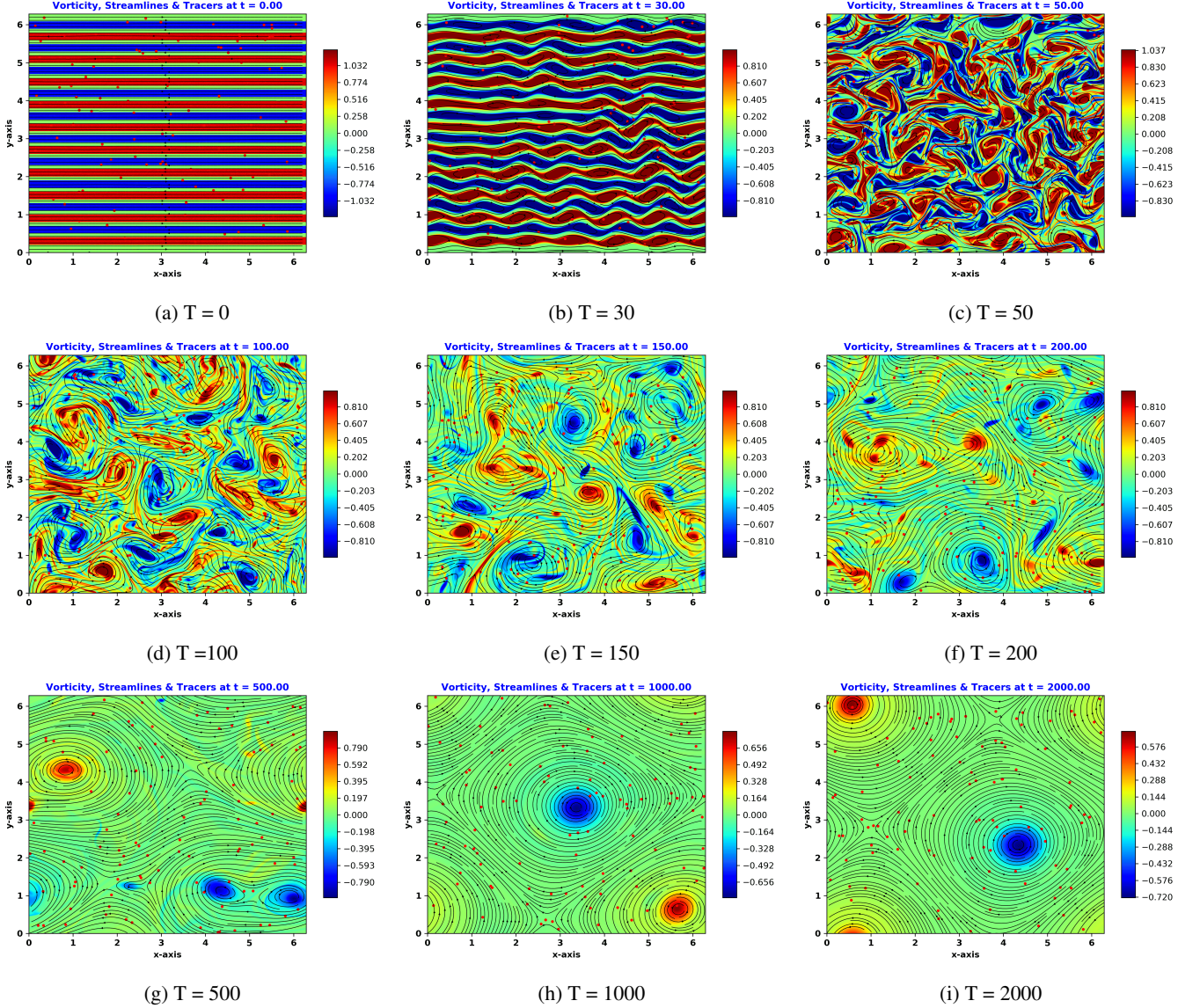


FIG. 6: This figure represents the vorticity and stream function evolution of turbulence and the associated tracer particles at various time instants from $T = 0$ to $T = 2000$. The turbulence is initiated by 16 strips of alternate vorticity that quickly evolves into turbulence where small scales merge into larger vortices and in steady state form two large scale dipole vortices in the background.

linear motion gradually develops in the y -direction, forming vortex rolls that undergo successive mergers. These mergers eventually suppress the initial ballistic x -motion at a relatively late stage. As a result, x -transport becomes subdiffusive due to the breakdown of coherent shear flow by vortex interactions and mixing, which reduce directed motion and promote localized displacement. In contrast, y -transport initially grows exponentially before transitioning into a slowly increasing, mildly superdiffusive regime, though it remains comparatively weaker. Throughout most of the vortex merging phase, x - and y -transports remain unequal, and the system remains strongly anisotropic, with dynamics predominantly governed by x -direction processes. Throughout the vortex

merger evolution, the total transport remains **subdiffusive**. Once the dipoles form which executes large-radius circular motions, tracers follow orbital paths around them, leading to largely trapped motion with limited net displacement and subdiffusive transport, where x - and y -transports are oscillatory and unequal.

We discuss the evolution of position pdf of the advected particles here which is uniformly distributed along x and y initially. As the flow starts, the initial x directed shear led ballistic particle motion leads to the initial uniform x direction pdf to broaden in time while the uniform y direction pdf remain uniform and flat due to limited y motion till a long time ($T = 100$). The pdf in the x direction initially becomes bi-

modal due to effect of the dominant x directed shear layers that persists for long times in this case. The x directed pdf is also assymetric around the mean position in the box length because more particles flow to the right side of the box due to the initial configuration of the shear layers. During this the dominant shear motion overshadows the fluctuating motions. As the vortices evolves, and interact, the flow becomes chaotic and the system eventually enters the turbulent regime. As the y directed turbulent fluctuations increase over longer times ($T = 250$), the y position distribution starts becoming normal distribution. The x pdf starts becoming a normal distribution at even longer times ($T = 500$ to $T = 750$). During these times, the posn pdfs do not match at all due to the anisotropic nature of the turbulence. Once the dipoles are formed, the particle position distributions in both the x and y directions remain nearly Gaussian and symmetric, and tries to close the gap between the two directions over time.

We discuss the evolution of velocity pdf here. As the flow starts, the x -velocity, v_x distribution develops a bimodal structure, with peaks near the mean shear velocities of the oppositely directed jets, and exhibits limited spread beyond these values. In contrast, the y -velocity v_y distribution remains sharply peaked around zero, reflecting the onset of small transverse fluctuations that are only beginning to emerge. As turbulence develops, the y -velocity distribution broadens as small-scale, random perturbations emerge across multiple scales, gradually adopting a Gaussian shape. Meanwhile, the initially shear-dominated x -velocity distribution also begins to spread due to growing fluctuations, and progressively transitions toward a normal distribution ($T = 250$, $T = 500$). The velocity distributions in both x and y directions also evolve toward Gaussian forms, reflecting the influence of multiscale, random fluctuations characteristic of fully developed turbulence. Once the dipoles are formed, the velocity distribution function tends to become bimodal again in this late-time regime. Each peak in the bimodal velocity PDF corresponds to one of the counter-rotating vortex populations, centered around $\pm v_{dp}$, where v_{dp} reflects the typical rotational velocity.

In the **four-strip case**, corresponding to a modest increase in vortex packing fraction, more vortex rolls emerge, reducing anisotropy and resulting in a comparatively more isotropic distribution across the domain than in the two-strip case, while the overall structure remains relatively sparse. While the spacing in the y -direction is reduced, these rolls evolve fully and take longer to interact with neighbors, establishing slow bidirectional merging and fluid deformation. As a result, turbulence sets in at a relatively late time ($T = 43$), leading to a relatively long-lived, stronger, and less anisotropic turbulent background, along with the rapid formation of more large-scale coherent vortices. The inverse cascade proceeds until the formation of the largest-scale dipoles, occurring at $T = 1000$. After the dipole formation, the dynamics is dominated by dipoles executing large-radius circular motions.

We discuss the transport of advected particles for the four strip case here. The shear-driven linear motion in the x -direction is reduced compared to the 2-strip case, while instability-driven nonlinear motion gradually develops in the y -direction, forming vortex rolls that undergo successive

mergers. These mergers eventually suppress the initial ballistic x -motion, though still at a relatively early stage. As a result, x -transport becomes subdiffusive somewhat earlier than in the 2-strip case, due to the breakdown of coherent shear flow by vortex interactions and mixing, which reduce directed motion and promote localized displacement. In contrast, y -transport initially grows exponentially before transitioning into a slightly faster-growing, more strongly superdiffusive regime. Throughout most of the vortex merging phase, x - and y -transports remain unequal, and the system becomes slightly less anisotropic than before, though the dynamics are still predominantly governed by x -direction processes. Throughout the vortex merger evolution, the total transport remains subdiffusive. After the dipole formation, the dynamics is dominated by dipoles executing large-radius circular motions, leading to oscillatory and unequal x - and y -transports. Particle motion becomes largely trapped, resulting in subdiffusive to normal diffusive transport.

We discuss the evolution of position pdf of the advected particles here which is uniformly distributed along x and y initially. As the flow starts, the initial x directed shear led ballistic particle motion leads to the initial uniform x direction pdf to broaden in time while the uniform y direction pdf remain uniform and flat due to limited y motion till $T = 75$. As the vortices evolves, and interact, the flow becomes chaotic and the system eventually enters the turbulent regime leading to a normal distribution in both x and y . After the onset of turbulence, the y -direction particle position distribution broadens, gradually approaching a Gaussian form and becoming comparable the x -component ($T = 1000$), indicating more isotropic turbulent mixing and diffusive transport. Once the dipoles are formed, the particle position distributions in both the x and y directions remain nearly Gaussian and symmetric, with close overlap between the two directions over time.

We discuss the evolution of velocity pdf here. As the flow starts, the x -velocity, v_x distribution develops a bimodal structure, with peaks near the mean shear velocities of the oppositely directed jets, and exhibits limited spread beyond these values. In contrast, the y -velocity v_y distribution remains sharply peaked around zero, reflecting the onset of small transverse fluctuations that are only beginning to emerge. As turbulence develops, the y -velocity distribution broadens as small-scale, random perturbations emerge across multiple scales, gradually adopting a Gaussian shape. Meanwhile, the initially shear-dominated x -velocity distribution also begins to spread due to growing fluctuations, and progressively transitions toward a normal distribution. The velocity distributions in both x and y directions also evolve toward Gaussian forms, reflecting the influence of multiscale, random fluctuations characteristic of fully developed turbulence. Once the dipoles are formed, the velocity distribution function tends to become bimodal again in this late-time regime. Each peak in the bimodal velocity PDF corresponds to one of the counter-rotating vortex populations, centered around $\pm v_{dp}$, where v_{dp} reflects the typical rotational velocity.

In the **eight-strip case**, which corresponds to a further increase in vortex packing fraction, a comparatively larger number of vortex rolls emerge than in the previous case, and they

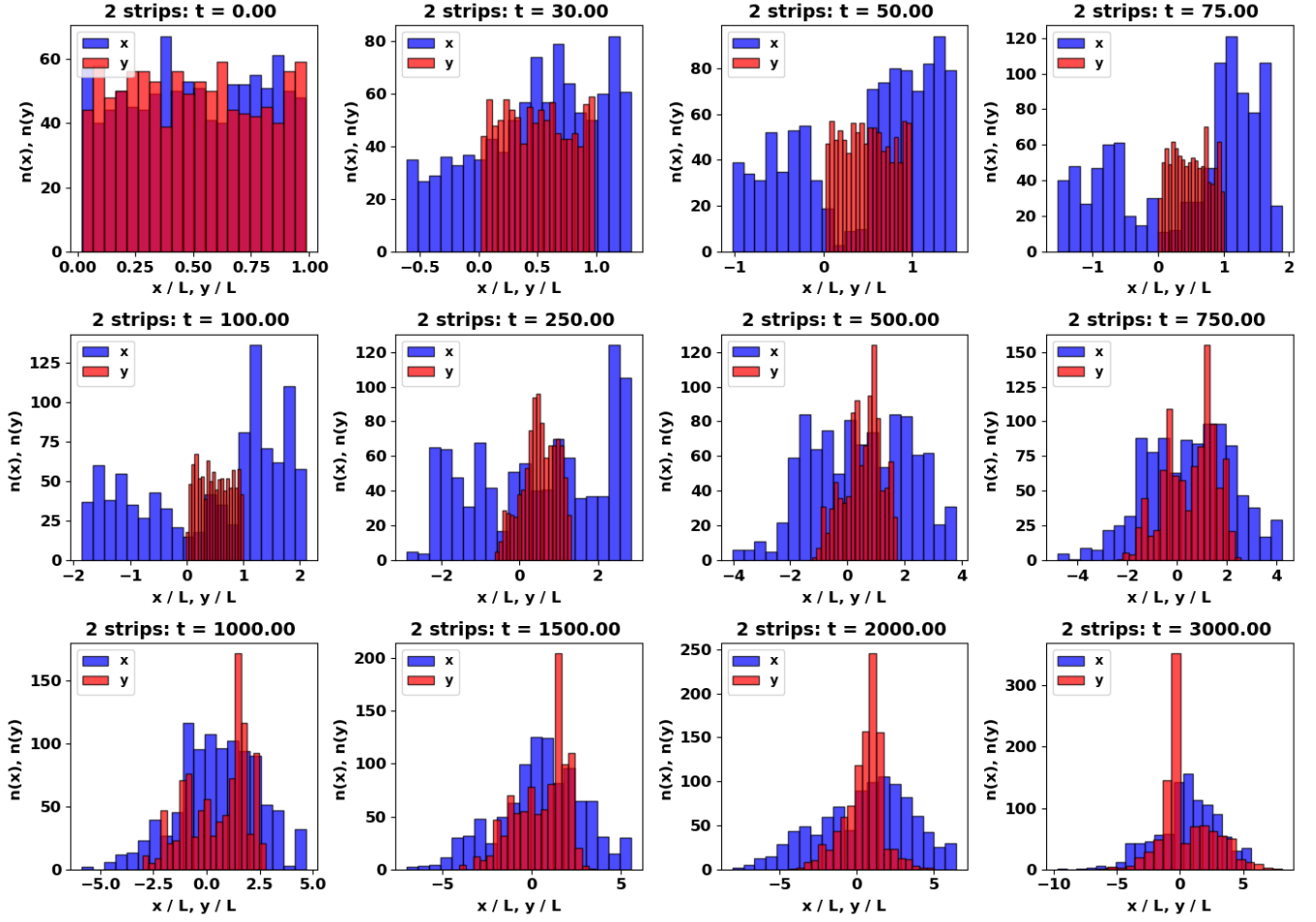


FIG. 7: Position distribution function evolution of tracer particles along x and y for 2-strip initialization.

are more densely and isotropically distributed across the simulation domain. While the spacing in the y -direction is further reduced, these rolls evolve fully and takes comparatively quick time to interact with neighbors, establishing quicker bidirectional merging and fluid deformation. As a result, turbulence sets in at a relatively early time ($T = 40$), leading to a relatively long-lived, stronger, and close to isotropic turbulent background, along with the rapid formation of further more large-scale coherent vortices. The inverse cascade proceeds until the formation of the larger-scale dipoles. In the eight-strip case, it takes the longest time to form dipoles. This is because towards the end of inverse cascading two isolated equal vortices of the same sign are formed and therefore take a long time to merge ($T = 900 - 2300$).

We discuss the transport of advected particles for a eight strip case here. As the flow starts, the shear-driven linear motion in the x -direction dominates which leads to x transport growth. This motion in the x -direction is further reduced compared to the 4-strip case, while instability-driven non-linear motion gradually develops in the y -direction, forming vortex rolls that undergo successive mergers. These merg-

ers suppress the initial ballistic x -motion at a relatively earlier stage. As a result, x -transport becomes subdiffusive somewhat sooner than in the 4-strip case, due to the breakdown of coherent shear flow by vortex interactions and mixing, which reduce directed motion and promote localized displacement. In contrast, y -transport initially grows exponentially before transitioning into a faster-growing, more strongly superdiffusive regime than in the 4-strip case. During the vortex merging phase, y -transport becomes equal to x -transport around $T = 450$ and remains slightly larger thereafter, indicating a system that is slightly less anisotropic than before. As the system continues to evolve and the turbulence coalesces into a few large-scale, slowly interacting coherent structures, y -transport also transitions to a subdiffusive regime due to prolonged particle trapping within these vortices. Throughout this vortex merger evolution, the total transport exhibits **normal diffusive** behaviour. The inverse cascade proceeds until the formation of the larger-scale dipoles. In the eight-strip case, it takes the longest time to form dipoles. This is because towards the end of inverse cascading two isolated equal vortices of the same sign are formed and therefore take a long time to

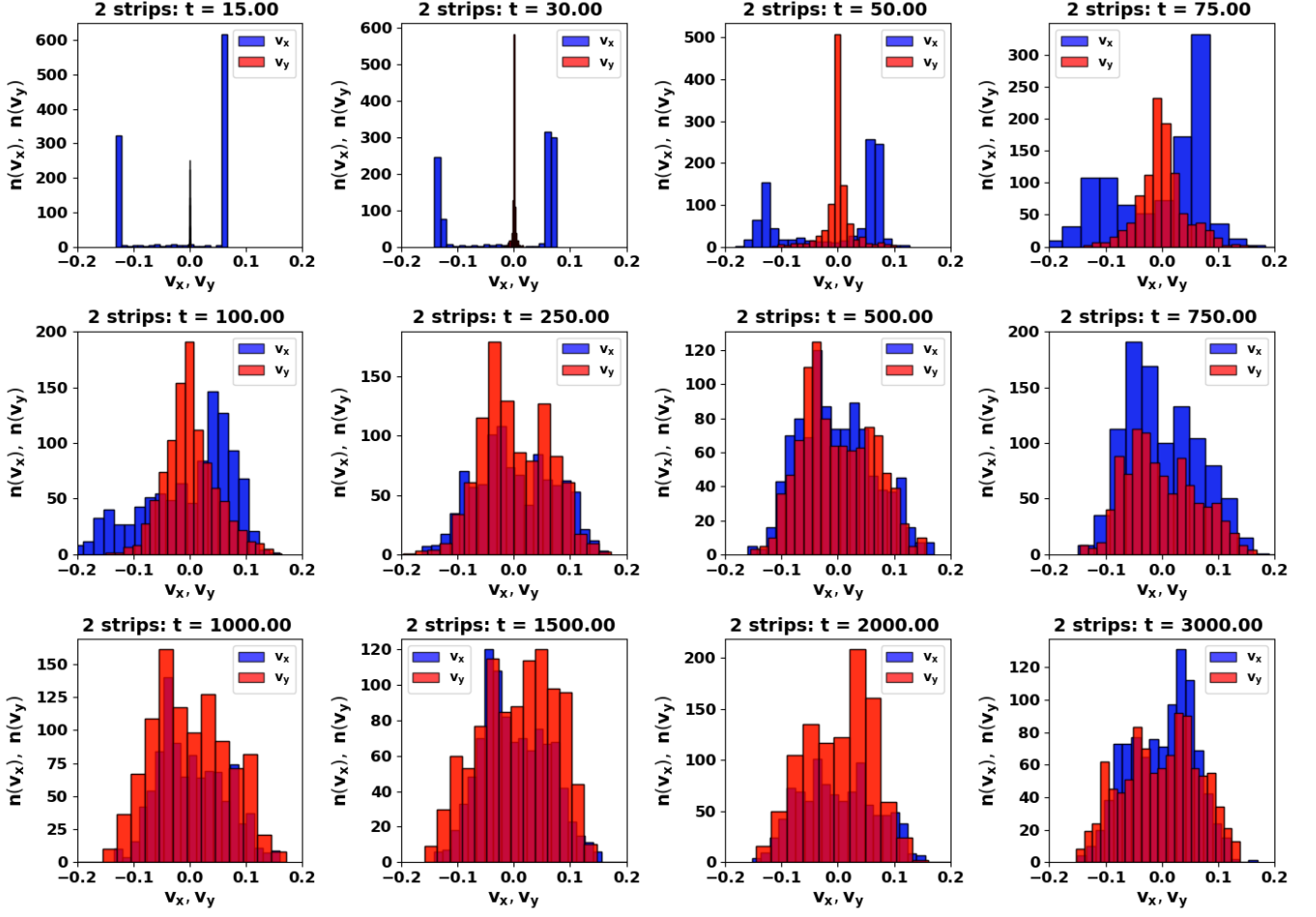


FIG. 8: Velocity distribution function evolution of tracer particles along x and y for 2-strip initialization.

merge ($T = 900 - 2300$). Thus these two vortices are in almost confined mode trying to merge but very weakly. These leads to subdiffusive particle transport.

We discuss the evolution of position pdf of the advected particles here which is uniformly distributed along x and y initially. As the flow starts, the initial x directed shear led ballistic particle motion leads to the initial uniform x direction pdf to broaden in time while the uniform y direction pdf remain uniform and flat due to limited y motion till $T = 50$. As the vortices evolves, and interact, the flow becomes chaotic and the system eventually enters the turbulent regime leading to a normal distribution in both x and y . After the onset of turbulence, the y -direction particle position distribution broadens, gradually approaching a Gaussian form and becoming comparable the x -component ($T = 450$), indicating more isotropic turbulent mixing and diffusive transport. Once the dipoles are formed, the particle position distributions in both the x and y directions remain nearly Gaussian and symmetric, with close overlap between the two directions over time.

We discuss the evolution of velocity pdf here. As the flow starts, the x -velocity, v_x distribution develops a bimodal struc-

ture, with peaks near the mean shear velocities of the oppositely directed jets, and exhibits limited spread beyond these values. In contrast, the y -velocity v_y distribution remains sharply peaked around zero, reflecting the onset of small transverse fluctuations that are only beginning to emerge. As turbulence develops, the y -velocity distribution broadens as small-scale, random perturbations emerge across multiple scales, gradually adopting a Gaussian shape. Meanwhile, the initially shear-dominated x -velocity distribution also begins to spread due to growing fluctuations, and progressively transitions toward a normal distribution. The velocity distributions in both x and y directions also evolve toward Gaussian forms, reflecting the influence of multiscale, random fluctuations characteristic of fully developed turbulence. Once the dipoles are formed, the velocity distribution function tends to become bimodal again in this late-time regime. Each peak in the bimodal velocity PDF corresponds to one of the counter-rotating vortex populations, centered around $\pm v_{dp}$, where v_{dp} reflects the typical rotational velocity.

In the **sixteen- and twenty-strip cases**, which correspond to the highest vortex packing fractions, the largest number of

vortex rolls emerge, distributed with the highest density and isotropy across the simulation domain. These closely spaced rolls do not have time to evolve into fully developed independent vortices and instead rapidly interact with neighboring vortices in both the x and y directions, triggering strong bidirectional mergers and fluid deformation almost immediately. As a result, turbulence sets in earliest in these cases, at $T = 36$ for the sixteen strip and $T = 33$ for the twenty strip configuration, leading to a persistent, strongest, and isotropic turbulent background populated by numerous coherent structures. The inverse cascade proceeds until the formation of the largest-scale dipoles, occurring at $T = 750$ for the sixteen-strip and $T = 600$ for the twenty-strip case. While in the sixteen-strip case, the dipoles execute small-radius circular motions, in contrast, in the twenty-strip case, the dipoles do not follow circular trajectories but keep moving in a linear fashion, indicative of Lévy flight-like dynamics.

We discuss the transport of advected particles for the sixteen- and twenty-strip cases here. As the flow starts, the shear-driven linear motion in the x -direction dominates which leads to large rise in x transport growth but comparatively much less than the 2, 4 and 8 strip cases. This motion persists for the shortest duration, while instability-driven nonlinear motion rapidly develops in the y -direction, leading to the formation of vortex rolls. These rolls undergo quick mergers, which strongly and rapidly suppress the initial ballistic x -motion. As a result, x -transport while still growing transitions from a ballistic to a subdiffusive regime quickly due to the breakdown of coherent shear flow by vortex interactions and mixing, which reduce directed motion and promote localized displacement. In contrast, y -transport initially grows exponentially before entering a rapidly increasing, strongly superdiffusive regime, driven by instability-enhanced mixing and flow deformation. The rise in these highly packed cases is much more than the previous low packing cases. At intermediate times, x - and y -transports become comparable ($T = 300$ for the 16-strip and $T = 250$ for the 20-strip cases) and remain closely matched, signaling the onset of a more isotropic turbulent regime. As the system evolves further and the turbulence condenses into a few large-scale, slowly interacting coherent structures, y -transport also transitions to a subdiffusive regime due to prolonged particle trapping within these large scale vortices. Throughout this vortex merger evolution, the total transport exhibits mildly superdiffusive behavior in the 16-strip case, and a stronger, more sustained superdiffusive regime in the 20-strip case, reflecting the extended duration and intensity of vortex interactions and mixing at higher initial vorticity packing. After dipole formation, the transport behavior diverges markedly between the two cases. In the sixteen-strip case, the dynamics is dominated by dipoles executing small-radius circular motions, leading to oscillatory and nearly equal x - and y -transports. Particle motion becomes largely trapped, resulting in subdiffusive transport. In contrast, in the twenty-strip case, the dipoles do not follow circular trajectories but moves diagonally across the simulation domain in a linear fashion. Therefore, both x - and y -transports grow monotonically in a superdiffusive manner, indicative of Lévy flight-like dynamics.

We discuss the evolution of position pdf of the advected particles here which is uniformly distributed along x and y initially. As the flow starts, the initial x directed shear led ballistic particle motion leads to the initial uniform x direction pdf to broaden in time while the uniform y direction pdf remain uniform and flat due to limited y motion till $T = 40$ and $T = 35$ reflecting the shear driven anisotropic nature of early-stage transport. As the vortices evolves, and interact, the flow becomes chaotic and the system eventually enters the turbulent regime leading to a normal distribution in both x and y quickly. After the onset of turbulence, the y -direction particle position distribution broadens, gradually approaching a Gaussian form and becoming comparable the x -component ($T = 250$), indicating more isotropic turbulent mixing and diffusive transport. Once the dipoles are formed, the particle position distributions in both the x and y directions become nearly Gaussian and remain symmetric, with close overlap between the two directions over time. In contrast, for the 20-strip case, although the distribution initially follows a similar Gaussian profile, it begins to develop heavy tails from $T = 2000$ onwards, indicating a departure from normality due to the onset of Lévy flight behavior.

We discuss the evolution of velocity pdf here. As the flow starts, the x -velocity, v_x distribution develops a bimodal structure, with peaks near the mean shear velocities of the oppositely directed jets, and exhibits limited spread beyond these values. In contrast, the y -velocity v_y distribution remains sharply peaked around zero, reflecting the onset of small transverse fluctuations that are only beginning to emerge. As turbulence develops, the y -velocity distribution broadens as small-scale, random perturbations emerge across multiple scales, gradually adopting a Gaussian shape. Meanwhile, the initially shear-dominated x -velocity distribution also begins to spread due to growing fluctuations, and progressively transitions toward a normal distribution. The velocity distributions in both x and y directions also evolve toward Gaussian forms, reflecting the influence of multi scale, random fluctuations characteristic of fully developed turbulence. Once the dipoles are formed, the velocity distribution function tends to become bimodal again in this late-time regime. Each peak in the bimodal velocity PDF corresponds to one of the counter-rotating vortex populations, centered around $\pm v_{dp}$, where v_{dp} reflects the typical rotational velocity.

As previously mentioned, the recent study of Biswas et al.²⁶ examined the long-term relaxation of two-dimensional incompressible decaying Navier–Stokes turbulence for varying vorticity packing fractions. It was demonstrated that the late-time relaxation state, as represented by the ω – ψ correlation, is quantitatively similar to the most probable state predicted by the statistical mechanical theory based on vortex patches (i.e., KMRS theory) for a tightly packed configuration (20 vortex strips)²⁶. In addition, the sinh–Poisson relation, KMRS predictions, and late-time DNS results all converge in the limit of a small packing fraction²⁶. The numerical results provide a clear and unambiguous transition in late-time two-dimensional decaying turbulence from the finite-size vortex description (KMRS theory) to the point vortex description as a function of initial circulation or vortex packing fraction. The

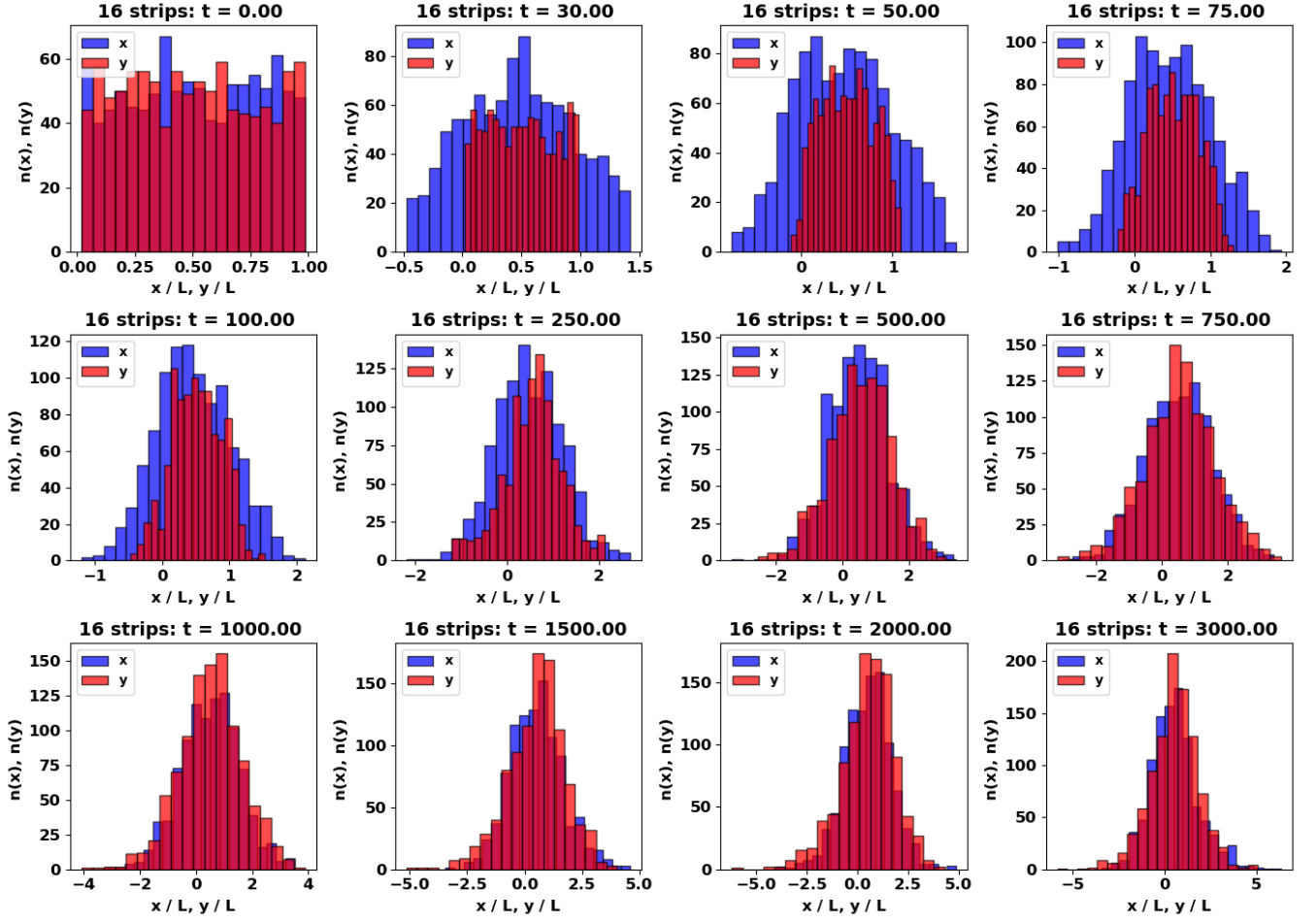


FIG. 9: Position distribution function evolution of tracer particles along x and y for 16-strip initialization.

present research, which builds upon the findings of the previous study²⁶, demonstrates that the initial vortex packing fraction has a significant impact on the turbulent transport properties. This illustrates a direct correlation between statistical vortex theories and turbulent transport. In the subsequent table (See Table I), the comprehensive transport characteristics of passive scalars are summarized.

IV. SUMMARY AND CONCLUSIONS

In this paper, we present results from numerical simulations of decaying two-dimensional hydrodynamic (2DHD) turbulence and its transport properties, initiated by Kelvin–Helmholtz instability with varying vorticity packing fractions. We examine how different vorticity packing fractions influence the evolution of turbulence across distinct regimes: the linear growth phase, turbulence development, and the motion of coherent dipolar vortices. To carry out this study, we developed a tracer particle solver integrated with our existing fluid solver, enabling us to extract particle trajec-

Initial Condition	Turbulence Onset	Turbulence Transport Evolution	Large Scale Structure Formation
2 strips	$T_{TO} = 45$	Sub diffusion High anisotropy	$T_D = 400$ subdiffusion
4 strips	$T_{TO} = 43$	Sub diffusion Less anisotropy	$T_D = 1000$ subdiffusion
8 stripes	$T_{TO} = 40$	Normal diffusion Slight Anisotropy	$T_D = 2300$ subdiffusion
16 stripes	$T_{TO} = 36$	Mild super diffusion Isotropy	$T_D = 750$ subdiffusion
20 stripes	$T_{TO} = 33$	Strong super-diffusion Isotropy	$T_D = 600$ subd- iffusion/Levy flight

TABLE I: Summary of turbulence evolution across different initial strip configurations

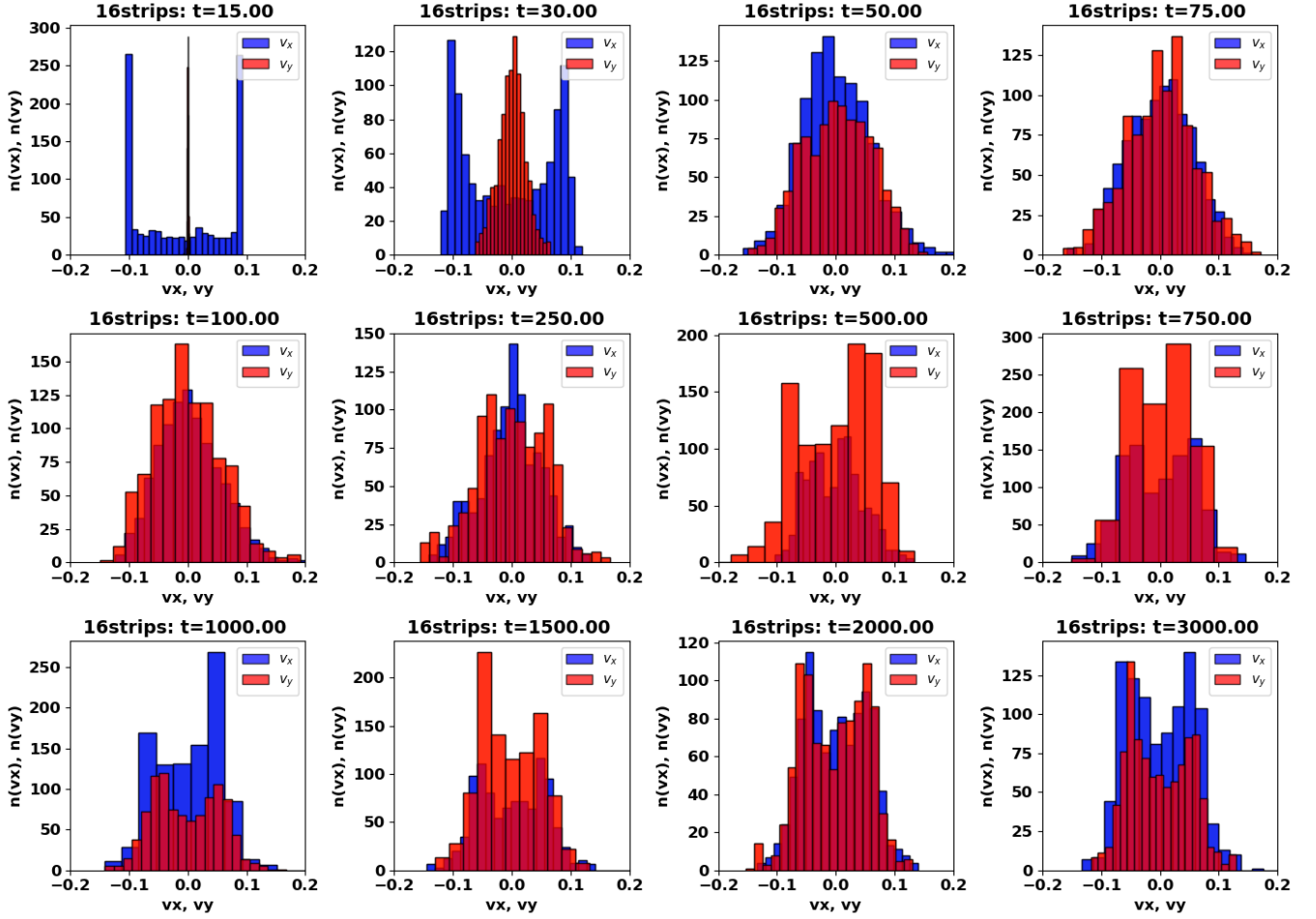


FIG. 10: Velocity distribution function evolution of tracer particles along x and y for 16-strip initialization.

ries from the simulations. We analyze absolute dispersion and the probability distribution functions of particle position and velocity to establish correlations across different diagnostics. Our findings reveal that the vorticity packing fraction plays a critical role in controlling the onset of turbulence, its nonlinear development, and the dynamics of the resulting steady-state dipolar vortex structures. The key highlights of our study are:

1) The KH shear instability triggers vortex roll formation and the onset of turbulence, where successive vortex mergers drive an inverse energy cascade from small-scale structures to larger coherent structures, ultimately forming the largest-scale dipoles that drift over long time. With increasing vorticity packing fraction, achieved by varying the initial strip configurations (2, 4, 8, 16, 20), the instability becomes stronger across the simulation domain, leading to earlier and more vortex mergers and the onset of turbulence that is more isotropic, intense, and persistent. The dipole motion is usually circular, with a radius that varies depending on the vorticity packing fraction, and in the highest-packing case, it exhibits long Lévy flights.

2) The associated tracer transport evolves from an initial

ballistic regime, dominated by x -directed shear, into an intermediate turbulence-driven phase—arising from the inverse cascade—which may be subdiffusive (2 and 4 strip cases), diffusive (8 strip case), or superdiffusive (16 and 20 strip cases), and finally into a late-time dipole-dominated regime, exhibiting either subdiffusive behavior (2, 4, 8, and 16 strip cases) due to trapped rotational motion or superdiffusive behavior during long Lévy flights (20 strip case), depending on the flow structure. With increasing vorticity packing fraction, the initial x -directed shear progressively weakens and becomes subdiffusive, while the y -directed instability-driven motion strengthens—transitioning from subdiffusive (2 and 4 strip cases), to diffusive (8 strip case), to superdiffusive—and dominates the total transport during the inverse cascade phase until x and y transport converge (20 strip case), marking the onset of more isotropic turbulent mixing. For the lowest packing fraction (2 strips), during this time the x and y transport has high difference indicating highly anisotropic turbulence that is also less persistent compared to the more enduring isotropic cases. For the dipole transport, in most situations, x and y transport remains oscillatory and subdiffusive due to

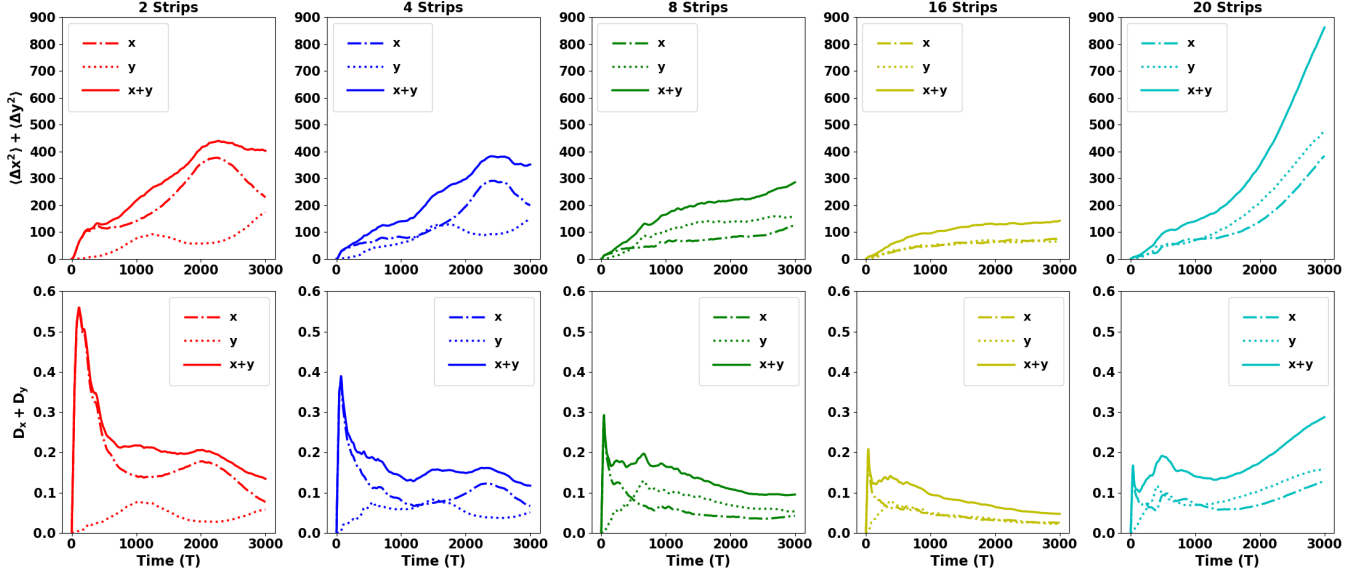


FIG. 11: This figure represents the transport of tracer particles in various cases of turbulence initiated by various packing fractions or strip numbers 2, 4, 8, 16, 20. The top row represents the mean square displacement evolution where as the bottom row represents the diffusion evolution. The dot dashed line represents the x transport, the dashed line represents the y transport and and solid line represents the total transport.

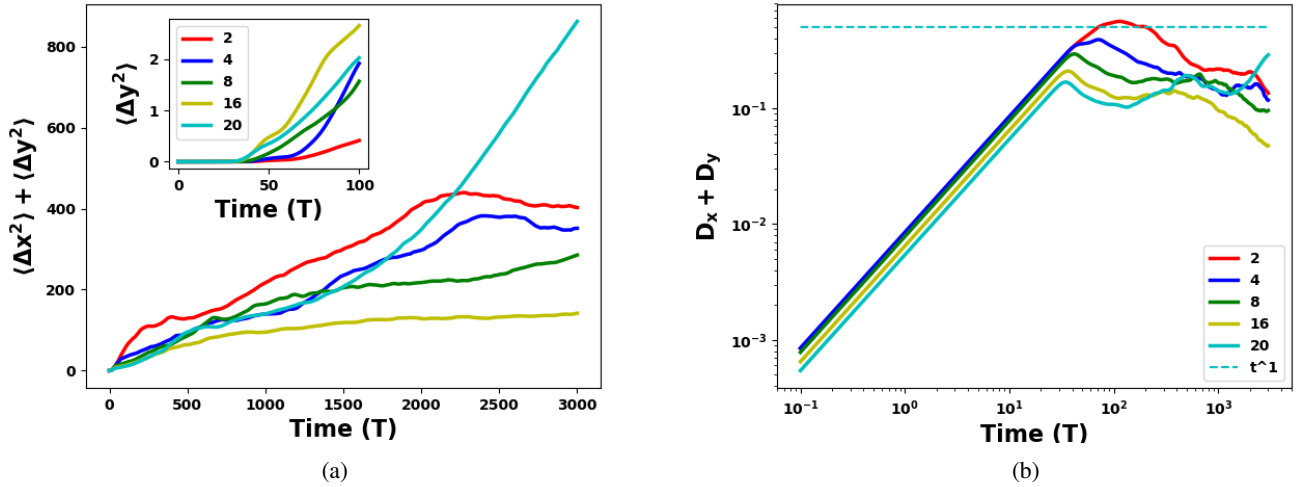


FIG. 12: Figure (a) represents the total transport (total mean square value evolution) of tracers particles during turbulence evolution in linear-linear axes. Different colors in these plots indicates transport in turbulence initiated by circulations of various packing fractions from low (2 strips) to high (20 strips). In this inset of this figure, only the linear regime of y transport is plotted. Figure (b) represents the same plot as Figure (a) in log-log axes.

dipole-induced circular motion, but in the 20 strip case, it is punctuated by anomalously superdiffusive long Lévy flights.

3) The initially uniform and flat position distribution function begins to broaden over time, first predominantly along the x direction and then along the y direction, eventually

approaching a normal distribution as turbulence develops. Tracer particles are advected in a seemingly stochastic manner, undergoing numerous small, random-like displacements driven by turbulent eddies. This motion resembles a random walk, causing the position probability distribution func-

tion to be normal distribution. As turbulence further evolves, the y -direction distribution catches up with the x -direction, and after dipole formation, both distributions remain Gaussian, symmetric, and nearly equal. Increasing the vorticity packing fraction accelerates this process: the x -direction distribution quickly becomes Gaussian, followed rapidly by the y -direction distribution, until isotropic turbulence is established and both directions exhibit nearly identical Gaussian profiles. At the lowest vorticity packing fraction, the initially uniform distribution in the x direction evolves into a more pronounced bimodal shape due to the long-lasting influence of shear. In contrast, the y -direction distribution remains largely unchanged during the early stages because of limited motion along y . Even at relatively long times, while the x and y distribution tends toward a Gaussian form, the x and y distributions do not become equal.

4) The velocity PDF initially appears bimodal in the x direction and nearly spike-like in the y direction due to limited y motion. As velocity fluctuations develop with turbulence, the distribution transitions to a normal form in both directions. At long times, however, it reverts to a bimodal shape, reflecting the dominance of dipole-induced counter-rotating vortex populations.

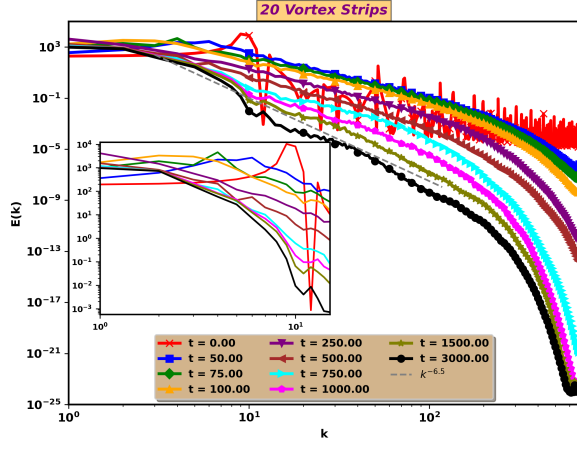
5) Overall transport is greatest in the lowest vorticity packing case (2 strips) due to the strong initial shear. However, at the highest vorticity packing fraction (20 strips), transport becomes unusually large again, driven by dipole motion characterized by Lévy flights.

6) The long-time transport properties clearly exhibit distinct behaviors at low and high vorticity packing fractions. This aligns with the steady-state statistical results reported by Biswas et al.²⁶, where the steady-state statistics vary according to KMRS theory, influenced by the initial vorticity packing fraction.

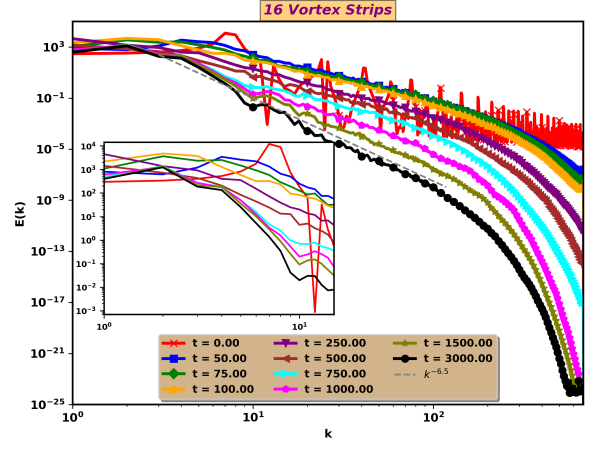
ACKNOWLEDGMENTS

The simulations and visualizations presented here are performed on GPU nodes and visualization nodes of the ANTYA cluster at the Institute for Plasma Research (IPR), India. The authors are grateful to the HPC support team of IPR for extending their help related to the ANTYA cluster.

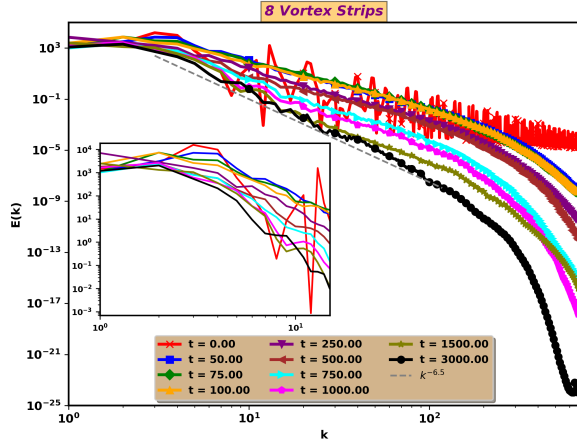
- ¹R. H. Kraichnan, "Inertial ranges in two-dimensional turbulence," *Physics of Fluids* **10**, 1417–1423 (1967).
- ²R. H. Kraichnan and D. Montgomery, "Two-dimensional turbulence," *Reports on Progress in Physics* **43**, 547 (1980).
- ³G. Boffetta and R. E. Ecke, "Two-dimensional turbulence," *Annual Review of Fluid Mechanics* **44**, 427–451 (2012).
- ⁴R. Corrado, G. Lacorata, L. Palatella, R. Santoleri, and E. Zambianchi, "General characteristics of relative dispersion in the ocean," *Scientific Reports* **7**, 46291 (2017).
- ⁵A. Hasegawa and M. Wakatani, "Plasma edge turbulence," *Physical Research Letters* **34** (1982).
- ⁶H. Xia and S. M. G., "Inverse energy cascade correlated with turbulent-structure generation in toroidal plasma," *Physical Research Letters* **34** (2011).
- ⁷M. Romé and F. Lepreti, "Turbulence and coherent structures in non-neutral plasmas," *Eur. Phys. J. Plus* **34** (2011).
- ⁸G. Boer and T. Shepherd, "Large-scale two-dimensional turbulence in the atmosphere," *Journal of the Atmospheric Sciences* **34** (1982).
- ⁹R. Corrado, G. Lacorata, L. Palatella, R. Santoleri, and E. Zambianchi, "General characteristics of relative dispersion in the ocean," *Nature* **34** (2017).
- ¹⁰P. Read, "The dynamics of jupiter's and saturn's weather layers: A synthesis after cassini and juno," *Annual Review of Fluid Mechanics* **34** (2024).
- ¹¹B. R. Sutherland, M. DiBenedetto, A. Kaminski, and T. van den Bremer, "Fluid dynamics challenges in predicting plastic pollution transport in the ocean: A perspective," *Phys. Rev. Fluids* **8**, 070701 (2023).
- ¹²M. Giovanni and C. Nakia, "Symmetries of the large scale structures of the universe as a phenomenology of a fractal turbulence: The role of the plasma component," *Symmetry* **34** (2024).
- ¹³M. R. Schoeberl and D. L. Hartmann, "The dynamics of the stratospheric polar vortex and its relation to springtime ozone depletions," *Science* **251**, 46–52 (1991).
- ¹⁴G. Haller and G. Yuan, "Lagrangian coherent structures and mixing in two-dimensional turbulence," *Physica D*, **147** (2000).
- ¹⁵G. I. Taylor, "Diffusion by continuum movements," *Proc. London Math. Soc., Ser. 2* **20**, 196 (1922).
- ¹⁶L. Richardson, "Atmospheric diffusion shown on a distance-neighbour graph," *Proc. R. Soc. London Ser. A* **110**, 709 (1926).
- ¹⁷P. Castiglione and A. Pumir, "Evolution of triangles in a two-dimensional turbulent flow," *Physical Review E*, **64** (2001).
- ¹⁸A. Pumir, B. Shraiman, and M. Chertkov, "Geometry of lagrangian dispersion in turbulence," *Physical Review Letters*, **85** (2000).
- ¹⁹E. Aurell, G. Boffetta, A. Crisanti, G. Paladin, and A. Vulpiani, "Growth of noninfinitesimal perturbations in turbulence," *PHYSICAL REVIEW Letters*, **77** (1996).
- ²⁰G. Haller, "Lagrangian coherent structures from approximate velocity data," *PHYSICS OF FLUIDS*, **14** (2002).
- ²¹M. K. Rivera, W. Daniel, and R. E. Ecke, "Lagrangian statistics and coherent structures in two-dimensional turbulence," *Physica D: Nonlinear Phenomena* **237**, 2090–2094 (2006).
- ²²A. Provenzale, A. Babiano, and B. Villone, "Single-particle trajectories in two-dimensional turbulence," *Annu. Rev. Fluid Mech.* **2002**, **34**, 115–42 (1995).
- ²³M. Wilczek, O. Kamps, and R. Friedrich, "Lagrangian investigation of two-dimensional decaying turbulence," *Physica D: Nonlinear Phenomena* **237**, 2090–2094 (2008).
- ²⁴O. Kamps and R. Friedrich, "Lagrangian statistics in forced two-dimensional turbulence," *Physical Review E* **78**, 036321 **78** (2008).
- ²⁵P. K. Yeung, "Lagrangian investigations of turbulence," *Annu. Rev. Fluid Mech.* **2002**, **34**, 115–42 (1921).
- ²⁶S. Biswas and R. Ganesh, "Long time fate of 2-dimensional incompressible high reynolds number navier-stokes turbulence: a quantitative comparison between theory and simulation," *Physics of Fluids* **34** (2022).
- ²⁷D. Montgomery, W. H. Matthaeus, W. T. Stribling, D. Martinez, and S. Oughton, "Relaxation in two dimensions and the 'sinh-poisson' equation," *Phys. Fluids A* **4**, 3 (1992).
- ²⁸G. Kuz'min, "Statistical mechanics of the organization into two-dimensional coherent structures," *Struct. Turbul.* **103**, 114 (1982).
- ²⁹J. Miller, "Statistical mechanics of euler equations in two dimensions," *Phys. Rev. Lett.* **65**, 2137 (1990).
- ³⁰R. Robert and J. Sommeria, "Statistical equilibrium states for two-dimensional flows," *J. Fluid Mech.* **229**, 291–310 (1991).
- ³¹G. Forgia, D. Cavaliere, S. Espa, F. Falcini, and G. Lacorata, "Numerical and experimental analysis of lagrangian dispersion in two-dimensional chaotic flows," *Scientific Reports* **34** (2023).
- ³²S. Biswas and R. Ganesh, "Pseudo-spectral solver versus grid-based solver: A quantitative accuracy test using gmhd3d and pluto4.4," *Computers & Fluids* **272**, 106207 (2024).
- ³³G. S. Patterson and S. A. Orszag, "Spectral calculations of isotropic turbulence: efficient removal of aliasing interactions," *Physics of Fluids* **14**, 2538–2541 (1971).
- ³⁴J. C. Adams, *On the Numerical Solution of the Differential Equation of Motion of a Particle* (Cambridge University Press, 1855).
- ³⁵F. Bashforth and J. C. Adams, *An Attempt to Test the Theories of Capillary Action* (Cambridge University Press, 1883).
- ³⁶NVIDIA Corporation, "cufft library," <http://developer.nvidia.com/cufft/> (Accessed 2025), gPU-accelerated Fast Fourier Transform library.
- ³⁷P. G. Drazin, "Discontinuous velocity profiles for the orr-sommerfeld equation," *Journal of the Atmospheric Sciences* **34** (1982).



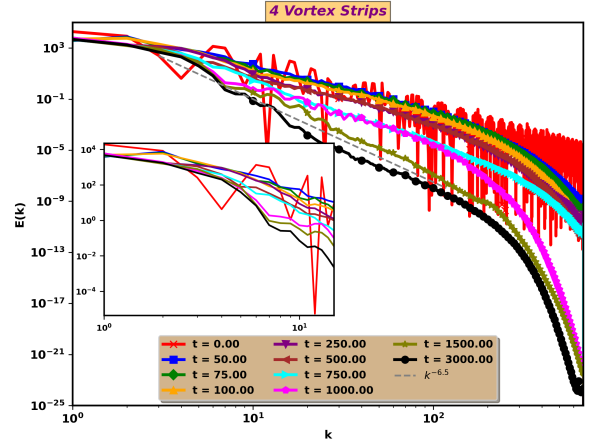
(a)



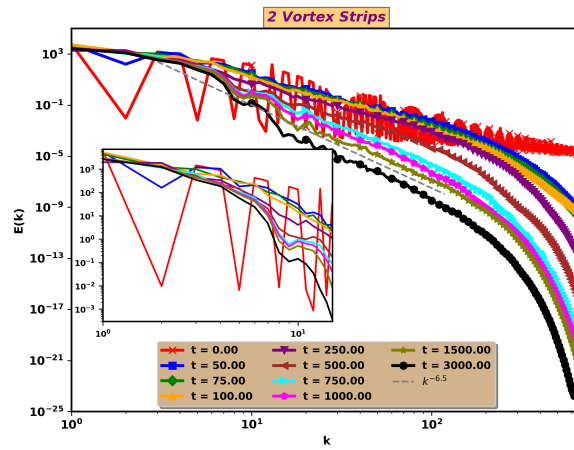
(b)



(c)



(d)



(e)

FIG. 13: Time Evolution of Turbulent Spectra

tion,” *Journal of Fluid Mechanics*, **10** (1961).

³⁸W. H. Press, S. A. Teukolsky, W. T. Vetterling, and B. P. Flannery, *Numerical Recipes: The Art of Scientific Computing*, 3rd ed. (Cambridge Univer-

sity Press, Cambridge, UK, 2007).